Liquid Crystals
Publication details, including instructions for authors and subscription information:
http://www.informaworld.com/smpp/title~content=t713926090

Simulation of texture formation processes in carbonaceous mesophase fibres

Dinesh Sharma[a]; Alejandro D. Rey[a]
[a] Department of Chemical Engineering, McGill University, Montreal, Quebec, Canada H3A 2B2,

Online publication date: 11 November 2010

To cite this Article Sharma, Dinesh and Rey, Alejandro D.(2003) 'Simulation of texture formation processes in carbonaceous mesophase fibres', Liquid Crystals, 30: 3, 377 — 389
To link to this Article: DOI: 10.1080/0267829031000089933
URL: http://dx.doi.org/10.1080/0267829031000089933

LIQUID CRYSTALS, 2003, VOL. 30, NO. 3, 377–389

Simulation of texture formation processes in carbonaceous mesophase fibres

DINESH SHARMA and ALEJANDRO D. REY*

Department of Chemical Engineering, McGill University, Montreal, Quebec, Canada H3A 2B2

(*Received 28 October 2002; accepted 9 December 2002*)

Carbon fibres are spun from carbonaceous mesophases using standard melt spinning techniques. These melt spun carbon fibres exhibit a set of distinct cross-sectional textures. Two widely reported textures in literature are the planar radial (PR) and planar polar (PP). This work uses a mesoscopic model, based on the classical Landau–de Gennes theory of liquid crystals adapted to carbonaceous mesophases, to elucidate the principles that control the texture formation processes. The model is able to capture the microstructure and the formation of the PR and PP textures. A phase diagram for classical PR and PP textures has been constructed in terms of temperature and fibre radius, thus establishing the processing conditions and geometric factors that lead to the selection of these textures. The multi-path formation process of the planar polar texture through defect splitting, direct planar polar formation, and defect annihilation has been thoroughly characterized. The results of this work provide new knowledge for optimization and control of mesophase carbon fibre textures.

1. Introduction

Carbonaceous mesophases are precursors used in the industrial manufacture of high performance carbon fibres. The carbonaceous mesophase is a discotic nematic liquid crystal which forms during the liquid phase pyrolysis of many hydrocarbons, including such practical materials as coal tar and petroleum pitch. The carbon fibres manufactured from mesophase pitches are more competitive than conventional fibres made from acrylic precursors in several application areas [1, 2]. The carbonaceous mesophase consists of disc-like molecules that display a discotic nematic liquid crystal (DNLC) phase. Figure 1 represents the molecular geometry, positional disorder and orientational order present in discotic nematic liquid crystals. The orientational order is represented by a unit vector field that describes the alignment of the anisotropic axis of the DNLC [3]. The unit vector field is referred to as a director $\mathbf{n}$ ($\mathbf{n} \cdot \mathbf{n} = 1$). The director gives the average preferred orientation of the unit normals $\mathbf{u}$ to the disc-like molecules as shown in figure 1.

The microstructure or the texture in mesophase carbon fibres is defined by the orientation distribution of the flat disc-like molecules. The conventional melt spinning of the mesophase pitches produces micrometer-sized cylindrical filaments whose cross-sectional area displays

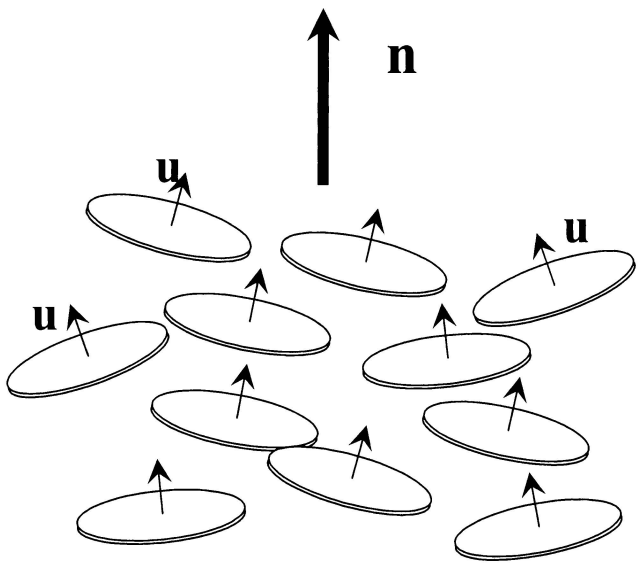

Figure 1. Definition of the director orientation of uniaxial discotic nematic liquid crystals (DNLCs). The director $\mathbf{n}$ is the average orientation of the unit normals to the disk-like molecules in a discotic nematic phase.

a wide variety of transverse textures [4] such as radial, onion, mixed and oriented core, to name a few. Figure 2 shows the two most commonly observed cross-sectional textures in mesophase carbon fibres, namely planar radial (PR) and planar polar (PP) [2]. The lines in the fibre cross-section represent the loci of the side view

*Author for correspondence;
e-mail: alejandro.rey@mcgill.ca

Liquid Crystals ISSN 0267-8292 print/ISSN 1366-5855 online © 2003 Taylor & Francis Ltd
http://www.tandf.co.uk/journals
DOI: 10.1080/0267829031000089933

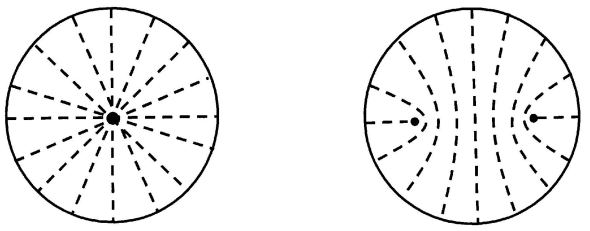

(*a*) (*b*)

Figure 2. Schematic of the two characteristic cross-sectional textures most commonly observed in mesophase carbon fibres. (*a*) Planar radial (PR), (*b*) planar polar (PP). The dashed lines indicate the disk trajectories, which are curves locally orthogonal to the director. The dark dots show the existence of defects.

of the disc-like molecules. Although the two textures, PR and PP, have been extensively investigated [4–7] a clear understanding of the transient process of texture evolution has been lacking. Transition among the two textures can be induced by changing the size of the fibre (geometric transition) or by changing the temperature (thermal transition). The aim of this paper is to investigate this transient process and understand the selection mechanisms that drive the texture formation process.

Computer simulations of liquid crystalline materials continue to be performed using macroscopic, mesoscopic, and molecular models [7–9]. Macroscopic models based on Frank free energy make use of the director equations but are not ideal for simulating dynamic transient texture formations starting from a random isotropic state subsequently quenched into the nematic phase. In addition to the orientation distribution of the two characteristic textures (i.e. PR and PP), another distinguishing feature is the presence of defects (disclinations) in the two texture. Defects in nematic liquid crystals are characterized by strength (1, 1/2 …) and its sign ($\pm$). The strength of a disclination determines the amount of orientation distortion and the sign corresponds to the direction of orientation rotation while circling the defect [10]. The defects in mesophase fibres arise due to the constraints of tangential boundary conditions and a planar two-dimensional (2D) orientation field. Planar radial texture has one defect of strength $s = +1$ at the axis of the fibre and the planar polar texture has two defects of $s = +1/2$ as shown by thick dark dots in figure 2.

Mesoscopic models based on the second moment of the orientation distribution function, here denoted by the symmetric traceless second order tensor **Q**, are well suited to capture the transient texture formation because defects are non-singular solutions to the governing equations. A very well established mesoscopic model is based on the Landau–de Gennes free energy [6, 7] and is used in this paper. The objectives of this paper are:

(1) To characterize, using well established theories and computer simulation, the transient texture formation of the characteristic textures namely, the planar radial (PR) and planar polar (PP).
(2) To characterize the driving forces, namely the long range energy (non-homogeneous) and the short range energy (homogeneous) that promote the selection of PR and PP texture.
(3) To study the transient processes involved in the formation of planar polar (PP) texture.

This paper is organized as follows. Section 2 presents the theory and the Landau–de Gennes governing equations and a brief discussion of the numerical methods. The numerical solutions to our model are presented in § 3, which includes a discussion of the transient evolution of the two characteristic PR and PP textures. Finally conclusions are presented.

2. Theory and governing equations

In this section we present the Landau–de Gennes theory of liquid crystals and the governing equations describing the mesophase fibre texture formation process.

2.1. *Definition of the tensor order parameter, director triad, and scalar order parameters*

The microstructure of DNLCs is characterized by the above mentioned second order symmetric traceless tensor, generally known as the tensor order parameter **Q** [11, 12].

$$\mathbf{Q} = S\left(\mathbf{nn} - \frac{1}{3}\delta\right) + \frac{P}{3}(\mathbf{mm} - \mathbf{ll}) \tag{1}$$

where the following restrictions apply:

$$\mathbf{Q} = \mathbf{Q}^T; \quad \mathrm{tr}(\mathbf{Q}) = 0; \quad -\frac{1}{2} \leqslant S \leqslant 1; \quad -\frac{3}{2} \leqslant P \leqslant \frac{3}{2} \tag{2}$$

$$\mathbf{n}\cdot\mathbf{n} = \mathbf{m}\cdot\mathbf{m} = \mathbf{l}\cdot\mathbf{l} = 1; \quad \mathbf{nn} + \mathbf{mm} + \mathbf{ll} = \boldsymbol{\delta}. \tag{3}$$

The uniaxial director **n** corresponds to the maximum eigenvalue $\lambda_n = 2S/3$, the biaxial director **m** corresponds to the second largest eigenvalue $\lambda_m = -(S-P)/3$, and the second biaxial director **l** ($=\mathbf{n}\times\mathbf{m}$) corresponds to the smallest eigenvalue $\lambda_l = -(S+P)/3$. The orientation is completely defined by the orthogonal director triad (**n**, **m**, **l**). The magnitude of the uniaxial scalar order parameter S is a measure of the alignment along the uniaxial director **n** and is given as $S = 3\,(\mathbf{n}\cdot\mathbf{Q}\cdot\mathbf{n})/2$. Similarly the biaxial scalar order parameter P, representing the degree of alignment along the biaxial director **m** can be expressed as $P = 3\,(\mathbf{m}\cdot\mathbf{Q}\cdot\mathbf{m} - \mathbf{l}\cdot\mathbf{Q}\cdot\mathbf{l})/2$. On the principal

axes, the tensor order parameter $\mathbf{Q}$ is represented as:

$$\begin{bmatrix} -\frac{1}{3}(S-P) & 0 & 0 \\ 0 & -\frac{1}{3}(S+P) & 0 \\ 0 & 0 & \frac{2}{3}S \end{bmatrix}. \tag{4}$$

According to equation (4), the model is able to describe biaxial ($S \neq 0$, $P \neq 0$), uniaxial ($S \neq 0$, $P = 0$) and isotropic ($S = 0$, $P = 0$) states.

2.2. *Landau–de Gennes mesoscopic model for liquid crystalline materials*

The Landau–de Gennes free energy density f of nematic liquid crystals (in the absence of surface terms and external fields) is defined as the sum of the homogeneous f_h (short range) and Frank elastic f_e (long range) contributions [12, 13]:

$$f = f_h + f_e \tag{5}$$

$$f_h = \frac{1}{2}A\,\mathrm{tr}(\mathbf{Q}^2) + \frac{1}{3}B\,\mathrm{tr}(\mathbf{Q}^3) + \frac{1}{4}C\,\mathrm{tr}(\mathbf{Q}^2)^2 \tag{6}$$

$$f_e = \frac{1}{2}L_1\mathbf{Q}_{\alpha\beta,\gamma}\mathbf{Q}_{\alpha\beta,\gamma} + \frac{1}{2}L_2\mathbf{Q}_{\alpha\beta,\beta}\mathbf{Q}_{\alpha\gamma,\gamma} + \frac{1}{2}L_3\mathbf{Q}_{\alpha\beta}\mathbf{Q}_{\gamma\delta,\alpha}\mathbf{Q}_{\gamma\delta,\beta} \tag{7}$$

where A, B and C are phenomenological coefficients (C must be positive in order for the homogeneous energy to have a minimum), and L_1, L_2 and L_3 are Landau coefficients which in the uniaxial state are functions of the three Frank elastic constants namely splay, twist, and bend (K_{11}, K_{22}, K_{33}), respectively. In the absence of biaxiality ($P = 0$) the relations between the Landau coefficients and the Frank elastic constants are [14]:

$$L_1 = \frac{3K_{22} - K_{11} + K_{33}}{6S^2}; \quad L_2 = \frac{K_{11} - K_{22}}{S^2}$$

and

$$L_3 = \frac{K_{33} - K_{11}}{2S^3}. \tag{8 a, b, c}$$

In the case of equal splay and bend as used in this paper the relations become:

$$L_1 = \frac{K_{22}}{2S^2}; \quad L_1 = \frac{K - K_{22}}{S^2}; \quad K = K_{11} = K_{33}. \tag{9 a, b}$$

Thermodynamic stability considerations impose the following inequality:

$$L_1 > 0, \quad 3L_1 + 5L_2 > 0. \tag{10}$$

In addition, for discotic nematic liquid crystals $L_2 < 0$, since twist distortions have the highest energy.

The governing equation describing the time evolution of the tensor order parameter $\mathbf{Q}$ follows a gradient flow model and is obtained by setting the variational derivative of the free energy equal to the rotational torque [15]:

$$-\gamma(\mathbf{Q})\frac{\mathrm{d}\mathbf{Q}}{\mathrm{d}t} = \left[\frac{\delta F}{\delta \mathbf{Q}}\right]^{[S]} = \left[\frac{\partial f}{\partial \mathbf{Q}} - \nabla\cdot\frac{\partial f}{\partial \nabla\mathbf{Q}}\right]^{[S]} \tag{11}$$

where the superscript [S] indicates a symmetric and traceless tensor, $\gamma(\mathbf{Q})$ is the rotational viscosity coefficient, and $\delta F/\delta\mathbf{Q}$ is the functional derivative of the total free energy density. For the phenomenological coefficients A, B, and C in the short range energy, Doi and Edwards [16] proposed the following expressions:

$$A = \frac{ckT}{2}\left(1 - \frac{U}{3}\right); \quad B = ckT\frac{U}{3}; \quad C = ckT\frac{U}{4}. \tag{12 a, b, c}$$

In the above expressions c is the number density of the discs, k is the Boltzman constant, and $U = 3T^*/T$ is the nematic potential, where T^* is a reference temperature just below the isotropic–nematic phase transition. Equation (11) represents three coupled non-linear parabolic reaction–diffusion equations for the three independent components of $\mathbf{Q}$: Q_{xx}, Q_{yy}, Q_{xy}. The director $\mathbf{l}$ is assumed to be along the fibre axis. Substituting equation (6) and (7) into equation (11) along with appropriate coefficients yields the following governing equations of $\mathbf{Q}(x, t)$ [16]:

$$\frac{\mathrm{d}\mathbf{Q}}{\mathrm{d}t} = -6\overline{D_r}\left\{\left(1 - \frac{U}{3}\right)\mathbf{Q} - U\left[\mathbf{Q}\cdot\mathbf{Q} - \frac{1}{3}(\mathbf{Q}:\mathbf{Q})\delta\right] + U(\mathbf{Q}:\mathbf{Q})\mathbf{Q}\right\} + 6\overline{D_r}\left\{\frac{L_1}{ckT}\nabla^2\mathbf{Q} + \frac{L_2}{2ckT} \times \left(\nabla(\nabla\cdot\mathbf{Q}) + [\nabla(\nabla\cdot\mathbf{Q})]^T - \frac{2}{3}\,\mathrm{tr}[\nabla(\nabla\cdot\mathbf{Q})]\delta\right)\right\} \tag{13 a}$$

$$\overline{D_r} \approx D_r\frac{1}{[1 - (3/2)\mathbf{Q}:\mathbf{Q}]^2}; \quad D_r = \frac{ckT}{6\eta} \tag{13 b, c}$$

where $\overline{D_r}$ is the microstructure-dependent rotational diffusivity, D_r is the pre-averaged rotational diffusivity or isotropic diffusivity independent of the microstructure and η is the viscosity of the material. The dimensionless

form of our governing equations can be written as:

$$\left(1-\frac{3}{2}\mathbf{Q}:\mathbf{Q}\right)^2\frac{\mathrm{d}\mathbf{Q}}{\mathrm{d}t} = -6\left\{\left(1-\frac{U}{3}\right)\mathbf{Q}-U\left[\mathbf{Q}\cdot\mathbf{Q}-\frac{1}{3}(\mathbf{Q}:\mathbf{Q})\delta\right] + U(\mathbf{Q}:\mathbf{Q})\mathbf{Q}\right\} + \frac{2L_1\times U}{H^2ckT^*}\left\{\tilde{\nabla}^2\mathbf{Q}+\frac{L_2}{2L_1} \times\left(\tilde{\nabla}(\tilde{\nabla}\cdot\mathbf{Q})+[\tilde{\nabla}(\tilde{\nabla}\cdot\mathbf{Q})]^T-\frac{2}{3}\,\mathrm{tr}[\tilde{\nabla}(\tilde{\nabla}\cdot\mathbf{Q})]\delta\right)\right\} \tag{14}$$

where quantities with superscript symbol ($\sim$) represents their dimensionless form. The first term on the right hand side of equation (14) represents the short range order energy contribution which governs the isotropic–nematic phase transition. The second term is the long range energy contribution that imposes an energy penalty for any spatial gradients (i.e. $\nabla\mathbf{Q}\neq 0$) present in the system. The dimensionless parameters that emerge from the above equation are $R=H^2ckT^*/2L_1$ $U=3T^*/T$ and $\tilde{L}_2=L_2/L_1$. The dimensionless parameter R represents the ratio of short range order elasticity and long range order elasticity [16], or equivalently the short range (internal) time scale and long range (external) time scale. Moreover $R(R\gg H^2/\xi^2)$ scales as the square of the ratio of the fibre radius (macroscopic length scale H or fibre radius in our case) to the molecular length scale (microscopic length scale ξ). The molecular length scale is given as $\xi=(L_1/ckT^*)^{1/2}$. When $R\leqslant 1$, long range energy dominates, spatial gradients are costly, and homogeneous states are selected. On the other hand, when $R\gg 1$, long range elasticity is insignificant with respect to short range order elasticity, and defects proliferate. In this work we show results for $0<R\leqslant 30$. The nematic potential U defined above indicates, for a uniaxial state, the thermal effects on the scalar order parameter S. An expression relating the nematic potential U to the scalar order parameter [15] is given by

$$S_{\mathrm{eq}}=\frac{1}{4}+\frac{3}{4}\left(1-\frac{8}{3U}\right)^{1/2}. \tag{15}$$

The third dimensionless parameter is $\tilde{L}_2=L_2/L_1$, the ratio of the two elastic constants and is a measure of the elastic anisotropy of the material. To satisfy the thermodynamic restrictions of equation (10), a value of $\tilde{L}_2=-0.5$ is used throughout for our simulations.

The set of governing dimensionless equations (14) are solved numerically on the unit circle. Initially ($\tilde{t}=0$) the system is isotropic, with $\mathbf{Q}\approx 0$ and $U=U_{\mathrm{iso}}<8/3$. This implies that the system is above the isotropic–nematic transition temperature and the isotropic phase is the only stable phase. The initial condition can be written as:

$$t=0,\quad \mathbf{Q}_{\mathrm{ini}}=S_{\mathrm{ini}}\left(\mathbf{n}_{\mathrm{ini}}\mathbf{n}_{\mathrm{ini}}-\frac{1}{3}\delta\right)+\frac{1}{3}P_{\mathrm{ini}}(\mathbf{m}_{\mathrm{ini}}\mathbf{m}_{\mathrm{ini}}-\mathbf{l}_{\mathrm{ini}}\mathbf{l}_{\mathrm{ini}}) \tag{16a}$$

$$\mathbf{n}_{\mathrm{ini}}=\begin{pmatrix}\cos(\zeta)\\ \sin(\zeta)\\ 0\end{pmatrix}\quad \mathbf{m}_{\mathrm{ini}}=\begin{pmatrix}\cos\left(\frac{\pi}{2}+\zeta\right)\\ \sin\left(\frac{\pi}{2}+\zeta\right)\\ 0\end{pmatrix}\quad \mathbf{l}_{\mathrm{ini}}=\begin{pmatrix}0\\ 0\\ 1\end{pmatrix} \tag{16b}$$

where S_{ini} and P_{ini} are the initial uniaxial and biaxial order parameters, respectively, generated randomly and $S_{\mathrm{ini}}\approx 0$, $P_{\mathrm{ini}}\approx 0$. The initial local orientation of the system is given by generating a set of random orthogonal unit vectors $\mathbf{n}_{\mathrm{ini}}$, $\mathbf{m}_{\mathrm{ini}}$, $\mathbf{l}_{\mathrm{ini}}$. The initial condition represents an isotropic state ($S=0$, $P=0$) with thermal fluctuations in order parameter (S, P) and orientation ($\mathbf{n}$, $\mathbf{m}$, $\mathbf{l}$). At the fibre boundary ($\tilde{r}=1$), Dirchlet boundary conditions are imposed on $\mathbf{Q}$, such that the state is uniaxial [$S=S_{\mathrm{eq}}$, see equation (15)] and the director is along the radial direction.

Equation (14) is a set of three coupled non-linear parabolic (reaction-diffusion) partial differential equations solved in a circle. The equations are solved using Galerkin Finite Elements with Langrangean linear basis functions for spatial discretization, and a predictor-corrector time adaptive scheme for time integration. Convergence and mesh independence were established in all cases using standard methods. As mentioned above, the Landau–de Gennes model for nematic liquid crystals has an internal length scale L_{i} and an external length scale L_{e}. The two length scales can be written as:

$$L_{\mathrm{e}}=H \tag{17a}$$

$$L_{\mathrm{i}}=\xi=\left(\frac{L_1}{ckT^*}\right)^{1/2} \tag{17b}$$

where H is the fibre radius, and ξ is the correlation length or the characteristic defect core size. The external length scale governs the director orientation ($\mathbf{n}$, $\mathbf{m}$, $\mathbf{l}$) whereas the internal length scale governs the scalar order parameter evolution (S, P). The model equations contain an internal time scale τ_{i} and an external time scale τ_{e}. The internal time scale governs the fast evolution of the scalar order parameters (S, P) and the external

time scale controls the slow orientation evolution of the directors (**n**, **m**, **l**). The slow and fast time scales can be expressed as:

$$\tau_i = \frac{\eta}{ckT^*} \tag{18 a}$$

$$\tau_e = \frac{\eta H^2}{L_1}. \tag{18 b}$$

The time adaptive integration scheme used for our computation is able to take into account the intrinsic stiffness of the system that arises from the disparity ($\tau_i \ll \tau_e$) between the slow and fast time scales.

3. Results and discussion

3.1. *Fibre textures*

The two characteristic textures obtained by numerical solution to the governing equation are the planar radial (PR) and planar polar (PP) textures. To visualize the computed texture, we represent the tensor field **Q** by an ellipsoid whose principal axes are proportional to its eigenvalue, and represent directions perpendicular to directors **n**, **m**, **l**; these three directions represent the average molecular orientation of the disc-like molecules. Figure 3 shows visualizations of representative computed textures, for $U = 6$, $\tilde{L}_2 = -0.5$. The left figure shows the PR texture for $H/\xi = 2.25$. The molecules are aligned in the radial direction (perpendicular) and a disclination of strength $s = +1$ forms at the centre of the fibre cross-section. The PR configuration is rotationally symmetric. The only deformation mode that exists in the PR texture is the bend mode K_{33}. The PP texture is shown on the right of figure 3, for $H/\xi = 5.0$. The PP texture configuration contains two defects of strength $s = +1/2$ collinear with the fibre axis. The PP texture has bend K_{33} as well as splay K_{11} modes of elastic deformation. In addition the PP texture has a perfectly aligned region between the two defects close to the centre of the fibre. The computed core structures for discotic nematic liquid crystals are consistent with the core structures for rod-like nematics [9]. Although not shown here, the defect core structures for DNLC have a biaxial ring and its centre is uniaxial, in agreement with rod-like nematics [9].

Figure 4 shows the texture phase diagram that defines the stability envelopes for the PR and PP textures as a function of dimensionless fibre size H/ξ and dimensionless reciprocal temperature U. The curved solid line represents the texture transition line. The phase diagram predicts that carbon fibres of smaller cross-section favour the PR texture whereas fibres of larger cross-section prefer the PP texture. It also predicts that the region of stability for the PR texture increases with increase in temperature (decrease in the nematic potential) until $U = 3.0$, after which the PR texture is stable for all fibre radii. Therefore if the carbon fibres are spun at higher temperature, they should exhibit a PR texture irrespective of the fibre radius. In constrast, if they are spun at lower temperature they should exhibit PP texture as well as PR texture depending upon the radius of the fibre. This is confirmed by experimental results [17]. In addition, the texture diagram is in agreement with the computations of Sonnet *et al.* [6], for rod-like nematic fibres. At low H/ξ the texture transition line is vertical, indicating that texture transformations are driven by size (geometric mode). At high H/ξ the texture transition line is horizontal, indicating that texture transformations are driven only by temperature (thermal mode). The existence of the geometric mode is due to the fact that when defect cores have the same

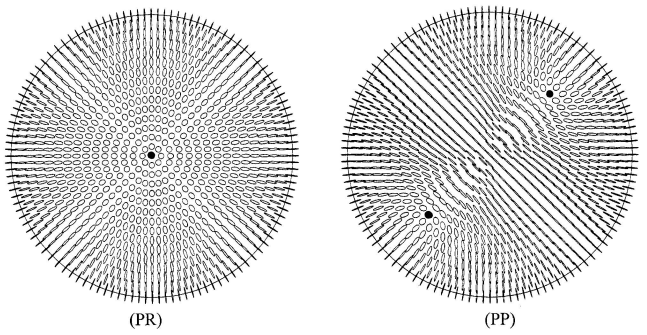

Figure 3. The two characteristic textures obtained as the solution to the governing equation. The planar radial (PR) with its characteristic disclination of strength +1 is shown on the left; the planar polar (PP) texture with two disclinations of strength +1/2 is shown on the right. The parametric conditions used are (i) for PR, $U = 6.0$, $\tilde{L}_2 = -0.5$, $H/\xi = 2.25$, (ii) for PP, $U = 6.0$, $\tilde{L}_2 = -0.5$, $H/\xi = 5.0$.

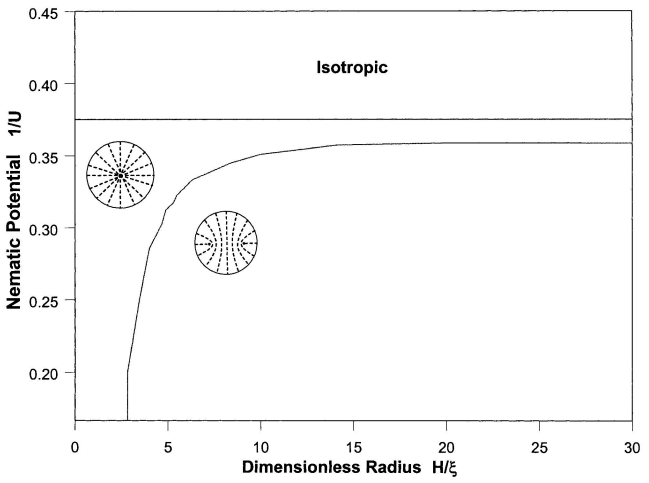

Figure 4. Phase diagram which predicts the type of solution for a given dimensionless temperature and dimensionless radius. The two stable characteristic textures observed are the planar radial (PR) and the planar polar (PP).

size as the fibre, then only one single defect can exist in the fibre, and the texture is then PR. The existence of the thermal mode indicates that the savings in long range elasticity due to the aligned central layer of the PP texture become insignificant at higher temperatures and thus a PR chimney arises.

3.2. *Texture formation processes*

In this section we characterize the transient structural processes and energetic changes that lead to the formation of the PP and PR textures.

3.2.1. *Planar radial texture formation*

Figure 5 shows a set of time snapshots of the director orientation $\mathbf{n}$ and the scalar order parameter S for four increasing times, corresponding to the PR texture, for $U = 6.0$, $\tilde{L}_2 = -0.5$, and $H/\xi = 2.45$. The scalar order parameter is given by a grey-scale plot, with white corresponding to $S = 0$, the black to $S = 1$. The evolution of S shows that order diffuses inward, as in a diffusion process. For $H/\xi = 2.45$, the time scale for orientation $\tau_{\mathbf{n}}$ is an order of magnitude smaller than the time scale τ_S the scalar order parameter.

Figure 6 shows the total dimensionless long range $\tilde{F}_e$ and the total dimensionless short range $\tilde{F}_h$ energies as a function of dimensionless time $\tilde{t}$, corresponding to the PR texture, for $H/\xi = 2.45$, and $U = 6.0$. The total dimensionless long range order elastic energy $\tilde{F}_e$ and short range energy $\tilde{F}_h$ are given by:

$$\tilde{F}_h = \int_0^{2\pi}\int_0^1 \left[\frac{1}{2}\left(1-\frac{U}{3}\right)\mathbf{Q}:\mathbf{Q} + \frac{1}{3}U\{\mathbf{Q}:(\mathbf{Q}\cdot\mathbf{Q})\} + \frac{1}{4}U\{\mathrm{tr}(\mathbf{Q}:\mathbf{Q})^2\}\right]\tilde{r}\,\mathrm{d}\tilde{r}\,\mathrm{d}\theta \tag{19}$$

$$\tilde{F}_e = \int_0^{2\pi}\int_0^1 [(\tilde{\nabla}\mathbf{Q})\vdots(\tilde{\nabla}\mathbf{Q})^T + \tilde{L}_2(\tilde{\nabla}\cdot\mathbf{Q})\cdot(\tilde{\nabla}\cdot\mathbf{Q})]\tilde{r}\,\mathrm{d}\tilde{r}\,\mathrm{d}\theta. \tag{20}$$

Figure 6 shows that the relaxation time for the long range elasticity is an order of magnitude smaller than that for the short range elasticity, in agreement with the results of figure 5. To explain why the director field relaxes faster than the order parameter we must consider the front evolution process that replaces the isotropic state with the nematic state. We shall perform the analysis assuming uniaxiality ($P = 0$). The front propagation solution for the scalar order parameter S in the uniaxial state and in a rectangular coordinate system is given by [18]:

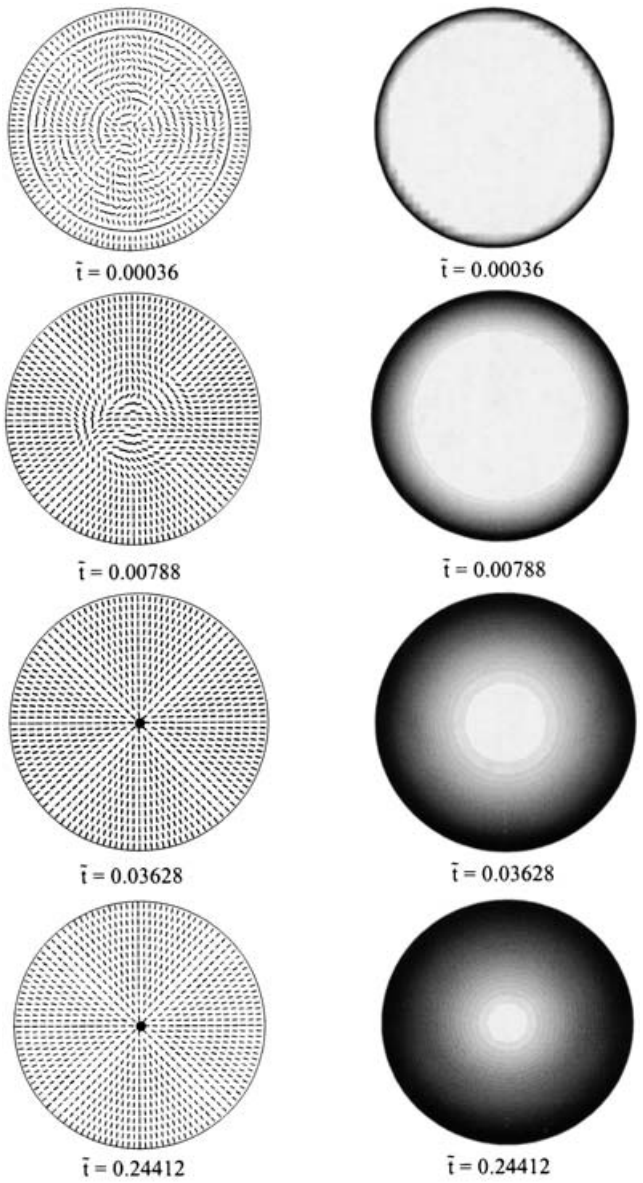

Figure 5. Transient evolution of the PR texture. The parametric conditions used here are $U = 6.0$, $H/\xi = 2.45$, $\tilde{L}_2 = -0.5$. Left column: orientation; right column: scalar order parameter.

$$S(y - vt) = \frac{S_{eq}}{2}\left\{1 - \tanh\left[\frac{XS_{eq}}{2}(\tilde{y} - v\tilde{t})\right]\right\} \tag{21}$$

$$v = 4\left(\frac{U}{3}\right)^{1/2}\left(\frac{\xi}{H}\right)\left[-\frac{1}{4} + \frac{3}{4}\left(9 - \frac{24}{U}\right)^{1/2}\right] \tag{22}$$

$$X = \left(\frac{U}{3}\right)^{1/2}\left(\frac{H}{\xi}\right) \tag{23}$$

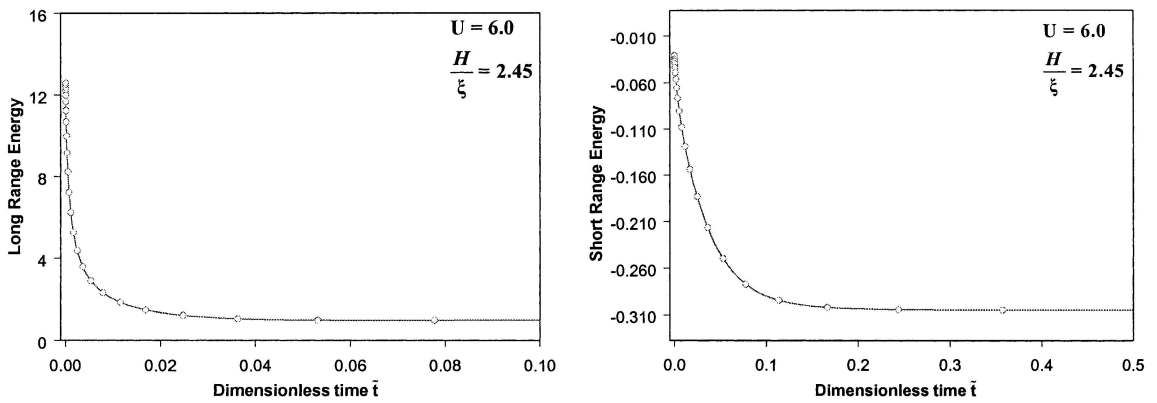

Figure 6. Time evolution of the long range energy and short range energy for $U = 6.0$, $H/\xi = 2.45$, $\tilde{L}_2 = -0.5$. The difference in the two time scales is not clearly visible since both are of the same order of magnitude for the parametric values used. The long range energy reaches a steady state at $\tilde{t} \approx 0.036$ whereas the short range energy reaches a steady state at $\tilde{t} \approx 0.24$.

where v is the dimensionless front speed, $\tilde{y}$ is the propagation direction, and $\tilde{t}$ is the dimensionless time. From this solution we estimate that the dimensionless time scale τ_S for the propagation of the scalar order parameter is:

$$\tau_S = \frac{1}{v} = \frac{1}{4\left(\frac{U}{3}\right)^{1/2}\left(\frac{\xi}{H}\right)\left[-\frac{1}{4}+\frac{3}{4}\left(9-\frac{24}{U}\right)^{1/2}\right]}. \tag{24}$$

For the values used in figure 6 ($U = 6$, $H/\xi = 2.45$) we find that equation (24) yields $\tau_S = 0.3$, while the actual computed value is approximately $\tau_S = 0.1$. Figures 5 and 6 show that the director dynamics is faster than the scalar order dynamics. This is a consequence of the fact that the scalar order parameter front penetrates an already oriented layer that forms ahead of the front. If that were not the case, the propagation would lead to defects and figure 6 shows that this is not the case. To compute the dimensionless time scale for the propagation of orientation $\tau_{\mathbf{n}}$ we assume that the layer thickness on which the director is aligned is of the order of the scalar order parameter front thickness d_f, which according to equation (21) is given, in dimensionless form, by:

$$d_f = \frac{2}{XS_{eq}}. \tag{25}$$

Then the dimensionless time scale $\tau_{\mathbf{n}}$ for propagation of orientation becomes:

$$\tau_{\mathbf{n}} = \tau_S(1 - d_f). \tag{26}$$

The computational results shown in figure 6 (left) show that $\tau_{\mathbf{n}} \approx 0.02$, while if we use equation (26) we find that $\tau_{\mathbf{n}} \approx 0.03$.

3.2.2. *Planar polar texture formation*

Computational modelling reveals that the formation process of the planar polar texture can occur through three different multi-staged modes, according to the magnitude of H/ξ, as follows.

3.2.2.1. *Defect nucleation–defect splitting–defect repulsion mode*

When $H/\xi < 10$, the computations show the evolution from the initial isotropic state to the final PP state is through the following processes:

isotropic state → PR (I) → defect split (II) → defect repulsion (III) → PP.

Figure 7 shows computed visualizations of the director orientation **n** (left column) and the scalar order parameter S (right column), for $U = 6.0$, $\tilde{L}_2 = -0.5$, $H/\xi = 3.16$, and four increasing dimensionless times. The figure shows that this mode involves the formation of the intermediate PR texture and then a classical defect split of a defect of strength $(s)s = +1$ into two defects of strength $s = +1/2$:

$$s = +1 \rightarrow 2s = +\frac{1}{2}. \tag{27}$$

Thus we call this process a defect nucleation-defect splitting-defect repulsion mode. The system takes this path when the parametric values used lie in the region where PR texture is metastable as given in the phase diagram constructed by Davis [19]. The phase diagram given in [19] gives, in addition to the stable textures shown in figure 3, textures that are metastable (steady state solutions to our governing equation but with higher energy). It is clearly visible in figure 7 that the system attains a planar radial texture with a defect of strength of $s = +1$ at the centre and then it transforms into two defects of strength $s = +1/2$. This path for the evolution of the PP texture is essentially a three-stage process. The early stage involves the formation of the intermediate PR texture, followed by an intermediate stage in which the topological transformation of the $s = +1$

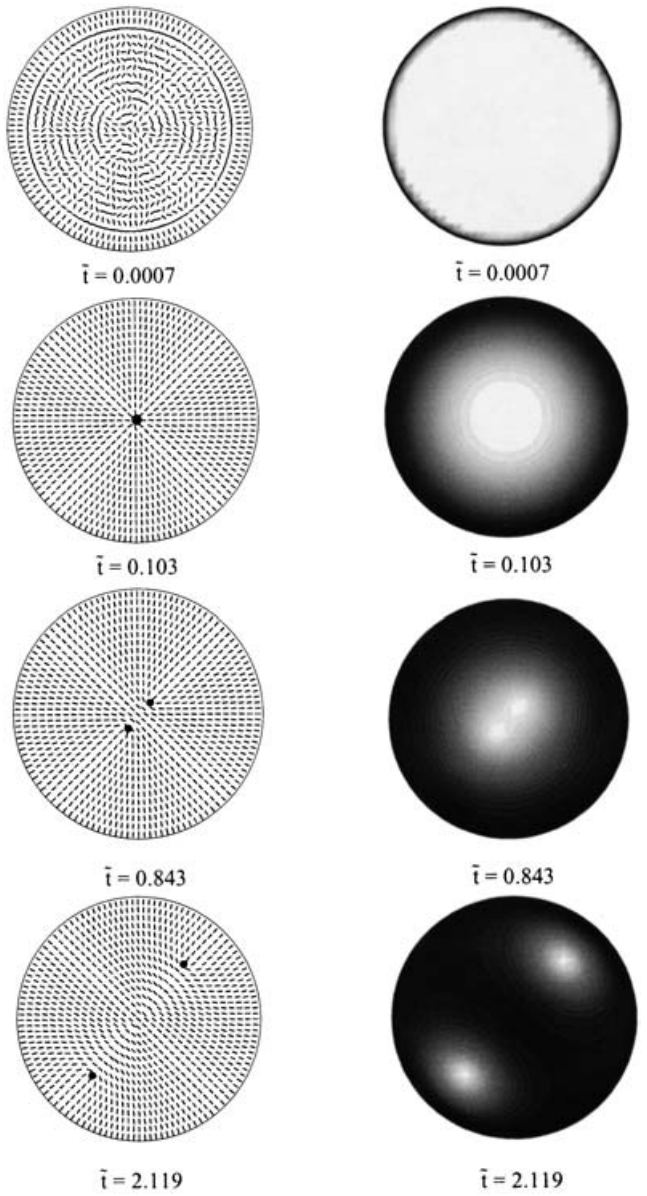

Figure 7. Transient evolution of the PP texture. The intermediate PR texture is clearly visible before the texture transforms into PP through defect splitting. The parametric conditions used here are $U = 6.0$, $H/\xi = 3.16$, $\tilde{L}_2 = -0.5$. Left column: orientation; right column: scalar order parameter.

defect into two defects of strength $s = +1/2$ occurs. The late (final) state is the separation of the two defects to their final equilibrium position by defect repulsion between the two equally charged $s = +1/2$ defects. The final separation distance l_f between the $s = +1/2$ pair in the PP texture has been determined analytically and is given by [20]:

$$\frac{l_f}{2H} = \frac{1}{\sqrt[4]{5}}. \tag{28}$$

The present formation process can be further understood by looking at the evolution of the dimensionless total short range order and dimensionless total long range order energies, defined above; see equations (19, 20). Figure 8 shows the total dimensionless long range order elasticity and total dimensionless short range order elasticity as a function of dimensionless time, for $H/\xi = 3.16$, 4.47, 10.0, and $U = 6.0$. We observe that there are essentially three stages (I, II, III) in the evolution of the long range elasticity. The long range elasticity in stage I of evolution reaches a minimum value. In stage II the long range elasticity increases until it reaches an intermediate plateau value. Finally in stage III there is further increase or decrease in the long range elasticity. In the early stage (i.e. at the bottom of the trough-like structure in the plot of long range elasticity) the microstructure is planar radial. In the intermediate stage the $s = +1$ defect splits into two $s = +1/2$ defects. As mentioned above, in the late stage the main phenomenon involved is the relocation of two defects at their final equilibrium position. In the time evolution of short range energy stage I with an exponential decrease is followed by stage II with a plateau, followed by a step-like decrease in stage III. The step-like decrease following stage II signals the beginning of the late stage. It is interesting to note that the onset of the late stage for both short range energy and long range energy evolution begins at almost the same time. The splitting of the $+1$ defect in a PR texture does not cause a change in the short range energy, and therefore at the end of the intermediate stage in the

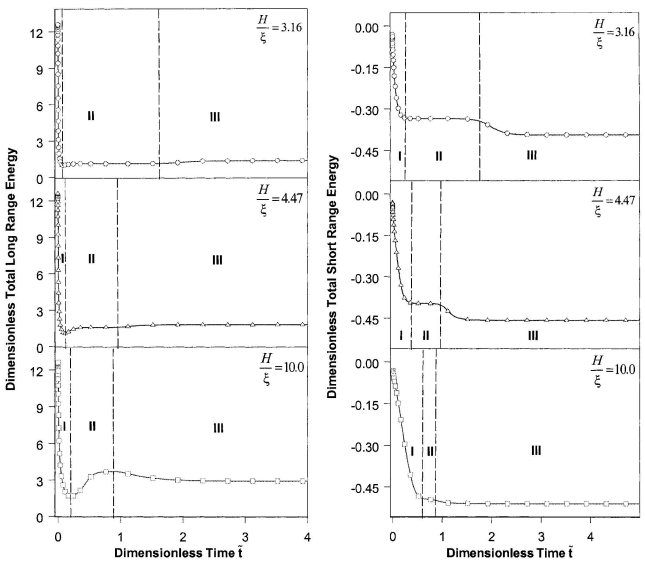

Figure 8. Long range and short range energy plots for different values of fibre radii H/ξ. The evolution of long range and short range energies follows three different stages (I, II, II). The dashed lines indicate the various stages which are not clearly visible in some cases.

short range the texture is planar polar but the two $+1/2$ defects are very close to each other. In other words the width of existence of stage II in the short range energy plot is proportional to the extent that the PR texture is metastable before it transforms to the PP texture. Thus from the plots we observe that for the given value of $U = 6.0$, the PR texture ceases to be metastable for $H/\xi > 10.0$.

In partial summary, for the present mode we make the following observations. First the system minimizes the elastic energy by forming a planar radial texture. According to the phase diagram (figure 4) the PR texture is stable at $U = 6$ for $H/\xi < 2.82$, but for the current values of $H/\xi > 2.82$, it is not. This implies a stronger force promoting uniaxiality that decreases the defect core radius and results in a higher energy of deformation, as given by the energy equation (29) for a defect of strength $s = +1$ [21]:

$$W = W_c + \pi K \ln\left(\frac{H}{r_c}\right) \tag{29}$$

where W_c is the core energy and r_c is the core radius. This is the reason for the increase in long range energy in the intermediate stage II. On the other hand the short range energy decreases by decreasing the defect core size. Therefore the system can reduce the total free energy by shrinking the defect core radius only up to a limit; beyond that the only way is by splitting the $s = +1$ defect into two $s = +1/2$ defects because the long range energy scales with the square of the defect strength. After the defect split there is a sudden drop in short range free energy due to the relocation of the two $s = +1/2$ defects after the split.

3.2.2.2. *Defect pair nucleation–defect repulsion mode*

When $10 < H/\xi < 30$, the computations show that the evolution from the initial isotropic state to the final PP state is through the following processes:

isotropic state → partial radial orientation (I)
→ defect nucleation (II) → defect repulsion (III) → PP.

Figure 9 shows orientation (left column) and order parameter (right column) for $U = 6.0$, $\tilde{L}_2 = -0.5$, $H/\xi = 14.15$, for four increasing dimensionless times. Figure 10 shows the total dimensionless long range free energy (left) and total dimensionless short range free energy (right) as a function of dimensionless time, for three increasing values of H/ξ, $U = 6.0$, and $\tilde{L}_2 = -0.5$. For this pathway the long range energy shows a three-stage process similar to the previous mode. The minimum of the long range energy (i.e. the lowest point of the trough-like shape in the long range energy plots in figure 10 at the end of stage I) no longer corresponds to a PR orientation configuration but has a texture that we will refer to as

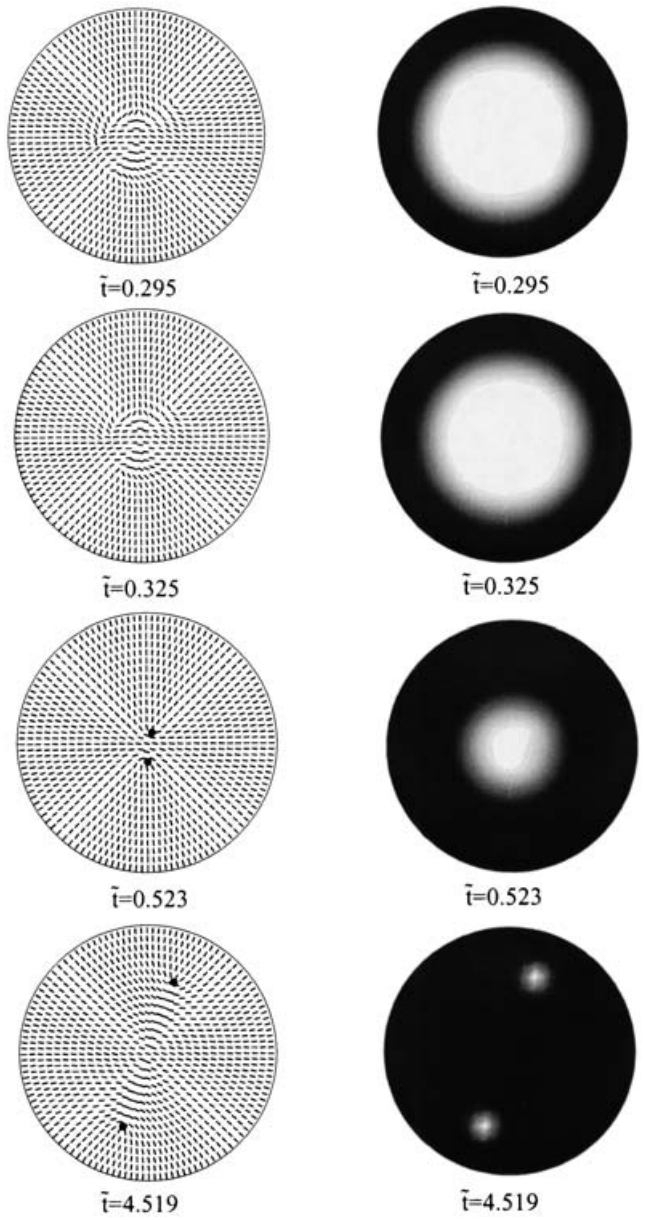

Figure 9. Second pathway for planar polar texture evolution without the formation and splitting of defect of strength $+1$. The parametric conditions used are $U = 6.0$, $H/\xi = 14.15$, $\tilde{L}_2 = -0.5$. Left column: orientation; right column: scalar order parameter.

isotropic core (IC), as shown in the top-most texture in figure 9 at $\tilde{t} = 0.2953$. The characteristic of the isotropic core texture is that there is a radial rim surrounding an isotropic core. The scalar order parameter S in the core region is non-zero but is very small for the parameters used in figure 9 ($U = 6.0$, $\tilde{L}_2 = -0.5$, $H/\xi = 14.15$). Once the long range energy has reached its minimum value (end of I) the scalar order parameter is still diffusing inwards, reducing the region of nucleation of the two $+1/2$ defects and thereby leading to an increase in the

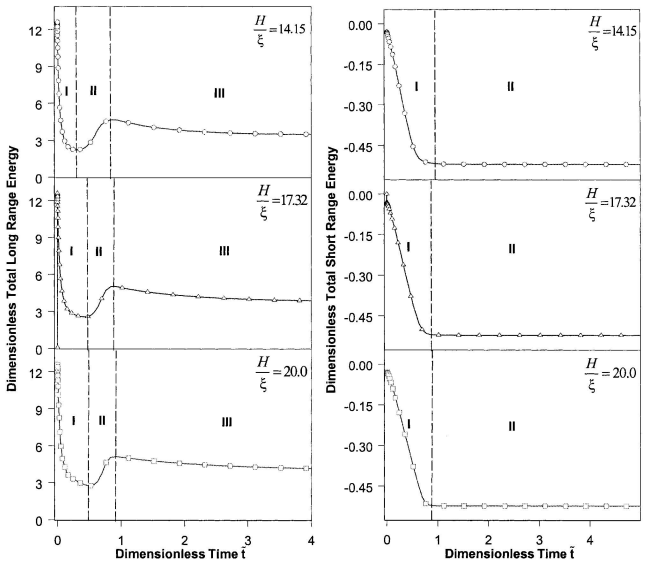

Figure 10. Long range energy and short range energy plots for different fibre radii H/ξ. The long range energy profile shows three distinct stages, as for first pathway, but short range energy does not show a step function-like drop and has only two stages (I and II).

long range elasticity. At the beginning, the diffusion of scalar order parameter, for this pathway to PP texture, is radially symmetric until the long range elasticity reaches its minimum value at the bottom of the trough. After that event, the radial symmetry of the scalar order parameter field is broken and there is anisotropic (non-axisymmetric) diffusion of the short range elasticity, as discussed below. The time scales for the orientation and scalar order parameter processes shown in figure 10 can be understood with the scaling given in equations (24, 26). For τ_s the computations give $\tau_S \approx 1$ and theory gives $\tau_S = 2.5$. For τ_n the computations give $\tau_n \approx 0.5$ and theory gives $\tau_n \approx 2.23$. Thus the theoretical scaling provides an explanation for the parametric dependence of the evolution.

Figure 11 shows two grey-scale visualizations of the scalar order parameter for $U = 6.0$, $\tilde{L}_2 = -0.5$, $H/\xi = 14.15$ (left), $H/\xi = 17.32$ (right), at the end of stage I. The figures show anisotropic diffusion of the scalar order parameter, with a finger-like front penetrating into the isotropic core that cleaves it into two separate isotropic 'daughter' cores. Another interesting phenomenon to note is that the time at which the long range energy reaches its local maxima (end of II) for transition into the third stage coincides with the short range energy reaching its steady state value. Finally the two $s = +1/2$ defects repel each other to an equilibrium position, leading to a small decrease in the long range energy.

Figure 12 shows computer visualizations of the orientation field (left) and scalar order parameter field (right) for

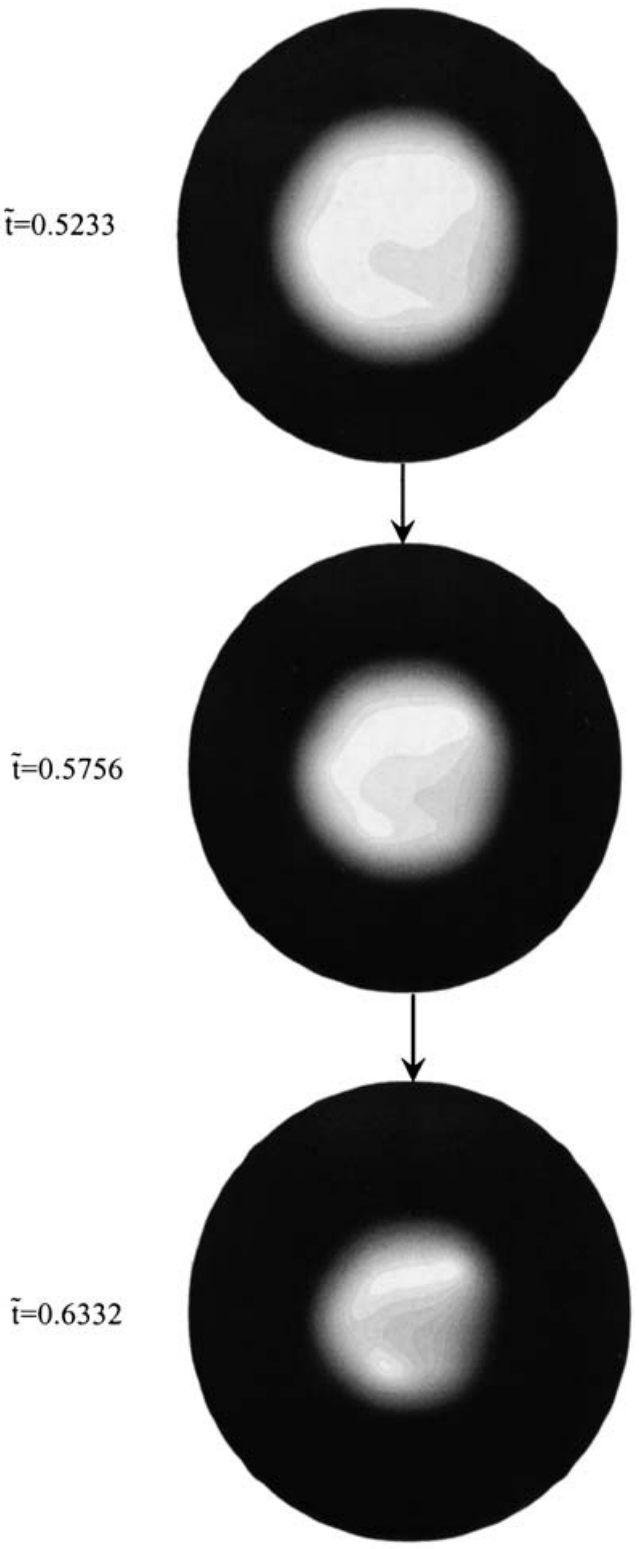

Figure 11. Time snap-shots exhibiting selective scalar order diffusion during the formation of planar polar texture for $H/\xi = 20$, $U = 6.0$ and $\tilde{L}_2 = -0.5$. The scalar order diffusion is anisotropic with a finger-like front moving into the isotropic core region, giving two defect cores.

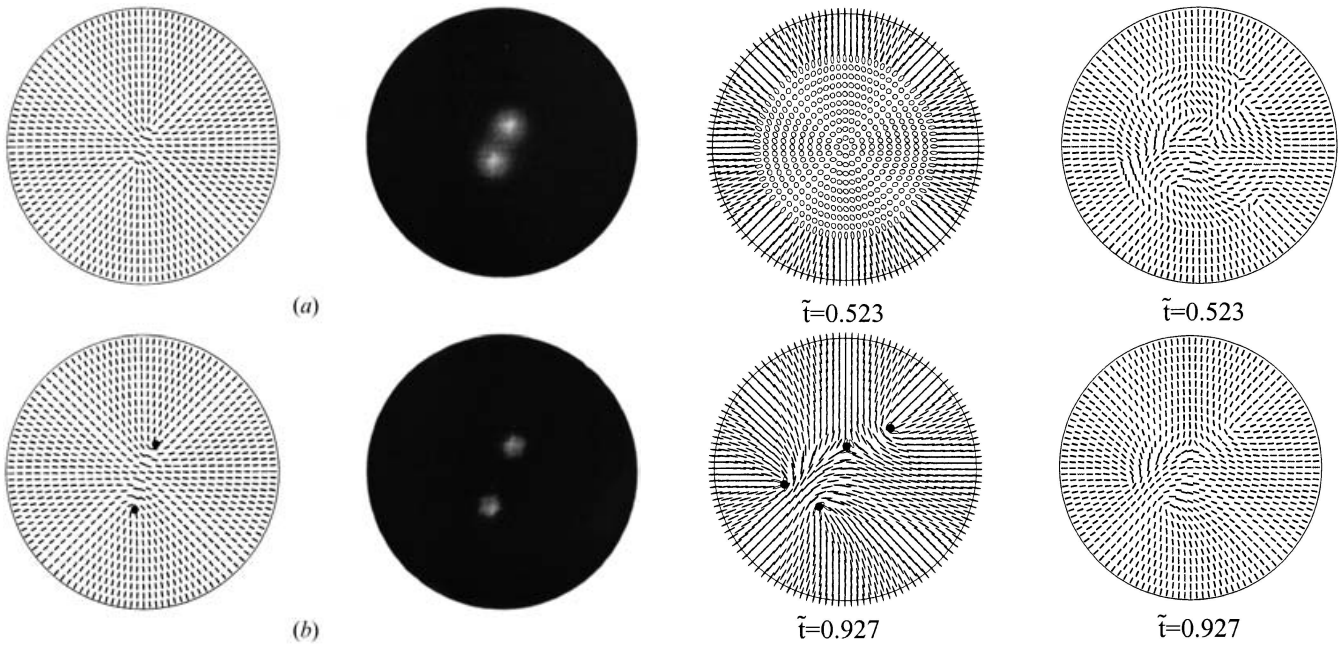

Figure 12. Demonstration that the distance of the nucleation of the two $+1/2$ defects increases with increasing fibre radius before they relocate to their equilibrium position. The value of H/ξ is 14.15 for (*a*) and 20.0 for (*b*). The value of U is 6.0 and $\tilde{L}_2 = -0.5$ for both cases.

$U = 6.0$, $\tilde{L}_2 = -0.5$, and $H/\xi = 14.15$ (*a*), $H/\xi = 17.32$ (*b*). The figure shows the nucleation distance of the $s = +1/2$ defect pair in the polar planar texture, before the repulsion process is activated. The figure clearly shows that the nucleation distance increases with increasing H/ξ, since the cleavage of the isotropic core into two daughter cores occurs on a larger core.

In partial summary, when H/ξ increases above a threshold ($H/\xi \approx 10$) the PR texture does not form but a pair of $s = +1/2$ defects nucleates instead; due to mutual repulsion the pair separates and eventully creates the classical PP texture.

3.2.2.3. *Defect nucleation–defect annihilation mode*

When $H/\xi > 30$, the computations show the evolution from the initial isotropic state to the final PP state is through the following processes:

isotropic state → defect nucleation (I)
→ defect annihilation (II) → defect repulsion (III) → PP.

As we move towards higher fibre radii ($H/\xi \gg 30$) for the same value of $U = 6.0$, there is an increase in the number of defects that form before the steady state polar texture is observed. This is clearly depicted in figure 13 showing the transient evolution of the planar polar texture at $U = 6.0$ and $H/\xi = 31.6$. Initially four defects are formed, followed by defect–defect interaction leading to the annihilation of two defects and eventually leaving two $+1/2$ defects. The defect annihilation reaction can be given as:

$$s = +\frac{1}{2} + s = -\frac{1}{2} \rightleftharpoons 0. \tag{30}$$

Figure 13. The formation of the PP texture through initial coarsening of multiple defects and consequent annihilation of two defects. The parametric values used in the above case are $U = 6.0$, $H/\xi = 31.6$ and $L_2 = -0.5$. The annihilation of two 1/2 defects is clearly visible at $t = 5.419$. Left: Ellipsoid representation. Right: Director representation. The dark dots represent the location of various defects.

This defect–defect interaction occurs because defects of opposite signs attract each other; the attractive force per unit length between two wedge disclinations of 1/2 strength is given by [11]:

$$\mathscr{F}_{12} = \frac{\pi K}{2d} \tag{31}$$

where K represents the Frank elastic constant in the case of one-constant approximation and d represents the distance between the two disclinations. In addition the fibre size is not too large to render long range elastic effects (like the defect interaction) negligible, as the attractive force reduces with the increase in distance between the defects.

Figure 14 shows the total dimensionless long range energy (left) and the total dimensionless short range energy (right) as a function of dimensionless time for $U = 6.0$, $\tilde{L}_2 = -0.5$, $H/\xi = 31.6$. The long range energy has four stages (I, II, III, IV) while the short range energy has two stages (I, II). The minimum of the long range energy corresponds to the topmost set of figures in figure 13, and can be characterized by an ordered boundary layer and isotropic central region (end of stage I for long range energy). In addition the director profile at this stage shows an apparent coarsening of multiple defects at future time. As the scalar order parameter diffuses inward some of the apparent defects in the director field become oriented and smooth out the sharp gradients. Eventually only four defects arise as the scalar order parameter diffuses inwards leading to an increase in the long range energy. The local maximum (end of long range stage II) following the minimum in the long range energy is characterized by four 1/2 defects (three defects of $+1/2$ and one defect of $-1/2$). This point corresponds to $t = 0.93$ in figure 14.

As indicated above, the time at which the long range energy reaches its local maximum is the same time at which the short range energy reaches its minimum steady state value. After this point the reduction in energy of the system is solely due to reduction in the long range energy. The local maximum in the long range energy is followed by its steady decay indicating the movement of the two 1/2 defects of opposite signs towards each other (long range stage III). Finally there is a sudden reduction in the long range energy (start of region IV), which is an indication of the annihilation of two half defects, followed by a small steady decrease denoting reorientation and relocation of the two remaining $s = +1/2$ defects. Moreover the long range energy reaches the steady state later than the short range energy because the long range order time scale (due to slow coarsening) is much larger than the short range order time scale for the fibre radius involved. The evolution is characterized by a rapid decrease due to propagation of order (I), followed by the essentially fully relaxed stage (II). Analysis with equations (24, 26) again correctly predicts the time scales of region I in the two energies.

4. Conclusions

A well established model based upon the classical Landau–de Gennes theory for liquid crystals has been used to model texture formation in mesophase carbon fibre. The model is able to predict the formation of planar radial and planar polar textures. The parametric conditions for their stability in terms of figure radius and temperature have been computed and represented in the form of a phase diagram. Lower temperature and thicker fibres tend to select the planar polar texture whereas thin fibres and higher temperatures tend to promote the emergence of the planar radial texture. This

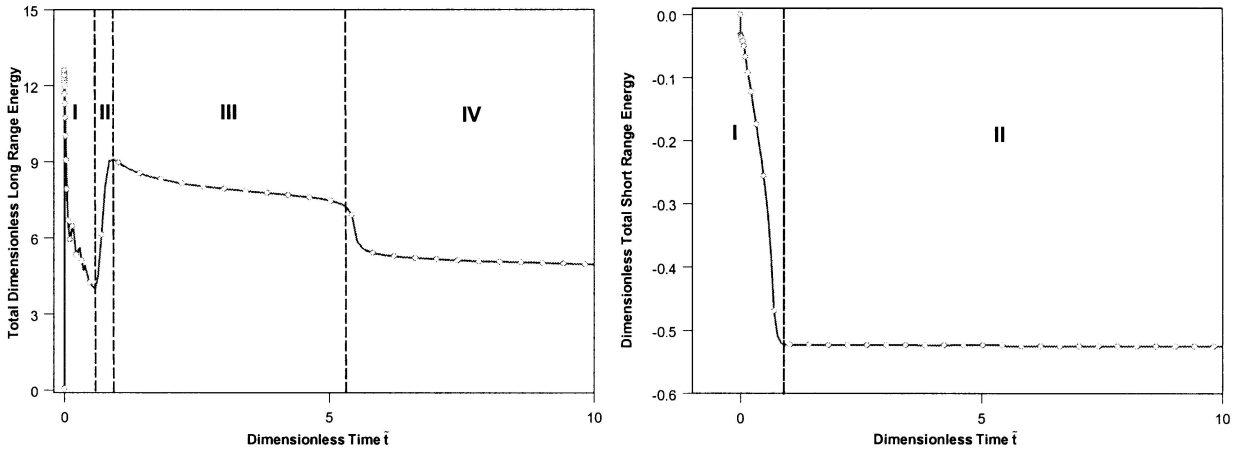

Figure 14. Time evolution of long range and short range energy for the formation of planar polar texture through defect annihilation. The parametric values used are $U = 6.0$, $H/\xi = 31.6$ and $L_2 = -0.5$. The long range energy exhibits an additional stage IV. A sudden reduction is visible in the long range energy at $\tilde{t} = 5.61$ where the two 1/2 defects combine to annhilate each other and leave only two $+1/2$ defects indicating onset of stage IV.

result is in agreement with the results of Sonnet *et al.* [6]. Furthermore a systematic analysis of the transient texture formation has revealed three different pathways for the formation of the planar polar texture depending on the parametric conditions used. For low temperature it is observed that with increasing fibre radius the formation mechanism for the planar polar texture changes from transformation via defect split from planar radial, to direct formation by nucleation of two $s = +1/2$ defects, to eventual formation of planar polar texture via defect annihilation. The results presented in this paper contribute towards a better understanding of the principles that control the cross-section texture selection during the melt spinning of mesophase carbon.

The authors gratefully acknowledge support from the NSF Center for Advanced Fibres and Films (CAEFF/NSF) at Clemson University.

References

[1] McHugh, J. J., 1994, PhD thesis, Clemson University.
[2] Peebles, L. H., 1995, *Carbon Fibres: Formation, Structures and Properties* (Boca Raton: CRC Press).
[3] Leslie, F. M., 1998, *Handbook of Liquid Crystals*, edited by D. Demus, J. Goodby, G. W. Gray, H.-W. Spiess and V. Vill (Weinheim: Wiley-VCH).
[4] Kralj, S., and Zumer, S., 1995, *Phys. Rev. E.*, **51,** 366.
[5] Burylov, S., 1997, *Sov. Phys. JETP*, **112,** 1603.
[6] Sonnet, A., Kilian, A., and Hess, S., 1995, *Phys. Rev. E.*, **52,** 718.
[7] Gartland, E. C., Jr., 1995, Technical Report ICM-199511-03, Institute for Computational Mathematics, Kent State University, USA.
[8] Smondyrev, A. H., and Pelcovits, R. A., 1999, *Liq. Cryst.*, **26,** 235.
[9] Sigillo, I., Greco, F., and Marrucci, G., 1998, *Liq. Cryst.*, **24,** 419.
[10] Zimmer, J. E., and White, J. L., 1982, *Advances in Liquid Crystals*, vol. 5 (New York: Academic Press).
[11] De Gennes, P. G., and Prost, J., 1993, *The Physics of Liquid Crystals*, 2nd Edn (Oxford: Clarendon Press).
[12] Priestley, E. B., Wojtowicz, P. J., and Sheng, P., 1975, *Introduction to Liquid Crystals* (New York: Plenum Press).
[13] Longa, L., Monselesan, D., and Trebin, H. R., 1987, *Liq. Cryst.*, **2,** 769.
[14] Beris, A. N., and Edwards, B. J., 1994, *Thermodynamics of Flowing Systems* (Oxford: Clarendon Press).
[15] Doi, M., and Edwards, B. J., 1986, *The Theory of Polymer Dynamics* (Oxford: Clarendon Press).
[16] Tsuji, T., and Rey, A. D., 1997, *J. non-Newtonian Fluid Mech.*, **73,** 127.
[17] Edie, D., 1999, private communication.
[18] Popa-Nita, V., Sluckin, T. J., and Wheeler, A. A., 1997, *J. de Physique II*, **7,** 1225.
[19] Davis, T. A., 1994, PhD thesis, Kent State University, USA.
[20] Yan, J., and Rey, A. D., 2002, *Phys. Rev. E*, **65,** 031713-1.
[21] Chandrasekhar, S., 1992, *Liquid Crystals*, 2nd Edn (Cambridge: Cambridge University Press).